This project has received funding from the European Union's ERA4Health Joint Transnational Call, "Research targeting development of innovative therapeutic strategies in cardiovascular disease" (CARDINNOV)

Co-funded by the European Union

D2.1 Detailed electrophysiological model of human atria.

PERSUADE

Project acronym	PERSUADE
Project number	ERA4HEALTHCVD-124
Project Title	PERsistent atrial fibrillation: Substrate tArgeteD stratEgy
Call/Topic identifier	ERA4HEALTH CARDINNOV
Project start date	April 1st, 2024

ERA4Health Partnership

D2.1 1) Average model to test mechanistic scenarios 2) Model personalization;

This project has received funding from the European Union's ERA4Health Joint Transnational Call, "Research targeting development of innovative therapeutic strategies in cardiovascular disease" (CARDINNOV)

Co-funded by the European Union

Work package	1
Deliverable No.	D2.1
Dissemination level	PU
Work package	WP2
Lead beneficiary	POLIMI
Version	2.0
Due date of deliverable	31/10/2025
Actual submission date	

Change log			
Version	**Date**	**Author**	**Reason for change**
1.0	30/10/2025	Chiara Celotto, José F. Rodriguez Matas	

Release log			
Version	**Date**	**Name and Organisation**	**Role**
1.0	28/11/2025	Etel Silva	Project coordinator

Table of Contents

ERA4Health Partnership

1 Introduction

In-silico modeling has emerged as a powerful approach to investigate complex cardiac phenomena that are often difficult or impossible to study directly in patients or even under experimental conditions. By integrating anatomical, electrophysiological, and biophysical data into computational frameworks, these models allow us to investigate the fundamental mechanisms governing cardiac electrophysiology across multiple spatial and temporal scales—from ionic currents in single cells to the propagation of electrical wavefronts in the three-dimensional atrial tissue.

Such multiscale models are particularly valuable in the context of atrial fibrillation (AF), where the onset and maintenance of the arrhythmia result from the interplay between structural remodeling, electrical heterogeneity, and various modulators. In-silico approaches enable controlled testing of these factors both in isolation and in combination, offering unique insights into how they shape atrial conduction patterns, generate vulnerable substrates, and influence the response to therapies.

Within this work package, we exploit these capabilities to build a detailed computational model of the atria capable of reproducing realistic electrical propagation and regional conduction properties. By integrating detailed electrophysiological descriptions, AF-induced remodeling, fibrosis-related conduction alterations, and realistic 3D atrial anatomy, the model reproduces physiologically accurate activation and propagation dynamics under both normal and pathological conditions. This model serves as a mechanistic platform to identify and characterize areas of slow or discontinuous conduction, which are often linked to the maintenance of the arrhythmia.

Furthermore, by integrating patient-specific data, characterizing abnormal substrate regions, and simulating both ablation and pharmacological interventions, the model supports hypothesis-driven investigation of how ablation outcomes are modulated by both structural and functional atrial remodeling.

Building upon this foundation, our efforts focus on identifying and disentangling the mechanisms through which key modulators—such as autonomic nervous system (ANS) activity, fibrotic remodeling, and the secretome released by epicardial adipose tissue—interact to shape atrial electrophysiology and foster arrhythmogenic substrates. This mechanistic insight ultimately supports the development of predictive, patient-tailored tools to guide treatment planning, optimize ablation strategies, and assess the efficacy of emerging pharmacological and neuromodulatory therapies.

Co-funded by the European Union

2 Average model to test mechanistic scenarios

Cellular electrophysiology. The atrial cellular electrophysiology was modeled using the human atrial cellular model developed by Courtemanche et al.(1). The Courtemanche model is a common-pool model, approximating the cytosol as a homogeneous compartment without considering local changes in intracellular ion concentrations. Hodgkin–Huxley ion channel formulations are used. The model includes the fast Na^+ current I_{Na}, the transient outward potassium current I_{to}, the ultrarapid delayed rectifier K^+ current I_{kur}, the rapid and slow delayed rectifier K^+ currents I_{Kr} and I_{Ks}, the inward rectifier K^+ current I_{K1} and the L-type Ca^{2+} current I_{CaL}. The Na^+ and Ca^{2+} background currents I_{bNa} and I_{bCa}, the Na^+/Ca^{2+} exchange current I_{NaCa}, the Na^+/K^+ pump current I_{NaK}, the sarcolemmal Ca^{2+} pump current IPMCA and the intracellular calcium handling were based on a previous (canine) model (2). The sarcoplasmic reticulum is divided into two compartments, one for uptake and one for release of Ca^{2+}. The Ca^{2+} uptake current Iup pumps Ca^{2+} into the sarcoplasmic reticulum and a leak current Ileak allows flow back into the intracellular space. The transfer current I_{tr} transports Ca^{2+} to the release compartment, where Ca^{2+} stores are emptied into the intracellular space by the Ca^{2+} release current I_{rel}. Regarding intracellular Ca^{2+} buffers, there are formulations for troponin, calmodulin and calsequestrin. The action potential (AP) shows a pronounced spike-and-dome morphology.

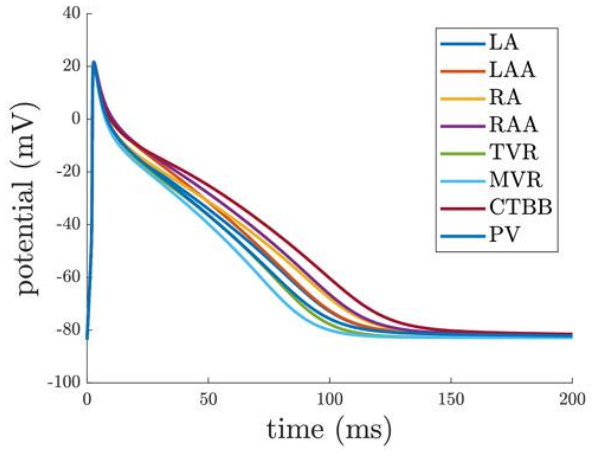

Figure 1: APs corresponding to the different electrophysiological regions in the 3D biatrial models.

3D anatomical and electrical properties. The bi-atrial anatomy was defined as in Ferrer et al. (3). The 3D anatomical models were discretized in a multi-layer mesh using linear hexahedral elements with an average edge length of 300 µm. The wall thickness varies between 600 and 900 µm, meaning that the wall was composed of 2 or 3 layers of hexahedral elements. This resulted in a total of 754.893

nodes and 515.010 elements. The models included detailed regional descriptions of fiber direction and functional heterogeneity, considering eight regions with different electrophysiological properties. The Courtemanche cellular model was adapted to represent different atrial regions by varying the ionic current conductances as in (3). These adjustments were made based on experimental observations regarding AP morphology and duration reported in several studies (4). The eight regions with different electrophysiological characteristics were: LA, right atrium (RA), left atrial appendage (LAA), right atrial appendage (RAA), PVs, tricuspid valve ring (TVR), mitral valve ring (MVR), crista terminalis (CT) and Bachmann bundle (BB). —each with specific adaptations of the Courtemanche model to match experimental AP morphology and duration. In Figure 1, the APs corresponding to these regions are shown. The myocyte-myocyte conductance values were calibrated to reproduce physiological total activation time (TAT), with longitudinal conductivity and transverse-to-longitudinal ratios adapted from Ferrer et al.(3). While the original study, on the base of anatomical and histological information, defined 21 anatomical regions characterized by the same CV, we considered a reduced subset of 10 that significantly influence P-wave and body-surface potentials. Therefore, for definition of the conductivity values, we considered the following atrial regions: LA, RA, PV, SAN, coronary sinus (CS), isthmus (IST), fossa ovalis (FO), CT, limb of the fossa ovalis (LFO), Bachmann bundle and pectinate muscles (BBPM). The defined conductivity values, reported in Figure 2, led to a TAT of 180 ms, in line with data reported in the literature for persistent AF (psAF) patients (5).

Region	L_{CV} (S/cm)	T/L_{CR}
RA	0.0030	0.35
CT	0.0085	0.15
PV	0.0017	0.50
BBPM	0.0075	0.15
IST	0.0015	1.00
SAN	0.0008	1.00
FO	0.0000	1.00
CS	0.0060	0.5
LA	0.0030	0.25
LFO	0.0075	0.15

Figure 2: Longitudinal conductivity (LCV) and transverse-to-longitudinal conductivity ratio (T/LCR) values for the different atrial regions

Tissue-scale propagation. Electrical propagation was modeled using the monodomain formulation, which couples the spatial spread of the action potential to the ionic dynamics governed by the Courtemanche-type ODE system. The monodomain model was chosen over the bidomain because it offers comparable accuracy for this application while being more computationally efficient, thus enabling large-scale bi-atrial simulations.

Simulation protocols and numerics. Single-cell models were paced at a fixed cycle length until reaching steady state, defined as less than 3% change in all state variables between consecutive cycles. The

Courtemanche model reached steady state after about 10 minutes of pacing, and these values were then used to initialize the tissue simulations. Numerical convergence was ensured by employing a temporal resolution of 0.005 ms for single-cell simulations and a spatial resolution of 0.02 cm for tissue propagation; mesh refinement was verified by confirming that further refinements altered longitudinal conduction velocity by less than 0.2%. Tissue-scale simulations were performed with ELVIRA(6), which solves the monodomain equations via a finite-element, operator-splitting scheme for computational efficiency.

2.1 Electrophysiological and structural remodelling and modulators

Atrial structural and functional changes may develop as a result of pathological systemic processes in cardiac conditions, including hypertension, valvular disease, heart failure, or AF itself (7). Electrical remodeling, including changes in APD and ionic mechanisms, occurs over a period of one to two weeks (8). In contrast, structural remodeling occurs over longer periods of atrial tachypacing (months) and is mostly irreversible (8,9). Structural remodeling in AF can manifest in various ways, including enlargement of the atrial chamber, cardiomyocyte hypertrophy, increased mismatch between the orientations of epicardial and endocardial myofibers, changes in atrial wall thickness, and most importantly, increased fibrotic or connective tissue content (10).

Fibrotic remodeling. Fibrosis is the hallmark of structural remodeling in AF, generally being significantly higher in AF patients compared to patients in sinus rhythm (SR) and in psAF compared to paroxysmal AF (pxAF) (11). Fibrosis remodeling is a multiscale process that occurs from the subcellular to tissue levels. It has been associated with GJs remodeling (12,13), fibroblast proliferation (14) and excess collagen deposition(11,13), all of which interfere with cardiac electrical propagation and slow conduction. Fibroblasts comprise around 10-15% of the myocardium volume, despite far outnumbering cardiomyocytes (15). While fibroblasts were traditionally considered passive structural cells, recent studies have shown that they can exhibit APs when electrically coupled to cardiomyocytes through GJ channels (16). Fibroblasts have been recognized to play a crucial role in modulating the electrical function of the myocardium (17,18). They can act as current sources or sinks during cardiomyocyte excitation, thus disturbing normal electrical propagation. Their proliferation has been associated with abnormal automaticity in the atria, where fibroblast-cardiomyocyte coupling can induce a depolarizing current during the diastolic phase and elicit APs (19). Additionally, fibroblasts can exert electrophysiological influences on neighboring myocytes (20), leading to changes in AP shape, resting membrane potential, AP upstroke velocity and conduction velocity (21,22).

Computational models of fibrotic atria have accounted for these remodeling characteristics, either separately or in combination. In our model, fibrotic remodeling was represented by focusing on gap junctions (GJ) remodeling and fibroblast proliferation. Increased collagen deposition—commonly modeled as non-conductive obstacles—was not included. In fibrotic regions, GJ conductance was reduced: fibroblast–fibroblast junctional conductance was set to one-quarter of myocyte–myocyte conductance (13,23,24), and when fibroblasts were coupled to myocytes, the junctional conductance was linearly adjusted depending on the number of fibroblasts coupled to a myocite. Fibroblast proliferation was represented by replacing myocytes with fibroblasts described by the active ionic model of MacCannell et al. (25), which includes a time- and voltage-dependent potassium current, an inward rectifier potassium current, a Na^+/K^+ pump, and a background sodium current. This approach captured the electrophysiological effects of fibrosis—slowed conduction and altered wavefront propagation.

In the biatrial model we modeled structural remodeling by including 20% diffuse fibrosis on the basis of histological studies reporting diffuse fibrosis percentages up to 40%, with a mean of approximately 20%, in psAF patients (11,26). These nodes were uniformly randomly selected and were assigned with fibroblast properties (MacCannell model). The myocyte-myocyte, myocyte-fibroblast and fibroblast-fibroblast conductivities were defined as described above.

AF-related remodeling. Electrophysiological remodeling also contributes to the development of a substrate that facilitates the tendency for persistence of AF (8). It induces changes in the biophysical properties of the Na^+, Ca^{2+} and K^+ currents, which lead to a shortening of the AP duration (APD) (8,27–31). The main affected ionic currents are: • I_{Na}: In patients with psAF, the peak I_{Na} density slightly decreases in the atrial myocardium (32). The steady-state activation shifts rightwards by about 10 mV (30). Furthermore, I_{NaL}, the late sodium current component, is significantly increased in psAF patients (32). •I_{CaL}: A reduction of about 50% in I_{CaL} density in psAF compared to that in SR is one of the most consistent findings in humans and animal models of AF (8,28,31). No changes have been reported in channel activation and inactivation properties (27). • I_{to} and I_{kur}: Human psAF has been strongly associated with a reduction in I_{to} density (28,30,33–36) and with downregulation of its α-subunit Kv4.3 (37). Different works have described a reduction in I_{kur} in psAF (34,36,38), along with a diminished expression of Kv1.5 in some studies (34,37). However, other studies have reported no changes in I_{kur} density (28,30,35). The inconsistency in I_{kur} function may result from different strategies to identify Ito and I_{kur}, i.e. peak and late current (38). The reduction in Ito and I_{kur} could explain the slight prolongation in the earlier phases of the action potential (31). • I_{Ks}: Caballero and

colleagues were the first to demonstrate that psAF significantly increases the amplitude of I_{Ks} in both atria (33). They suggested that the increase in I_{Ks} could contribute to psAF-induced shortening of APD and could further promote fibrillatory conduction, especially with its accumulation at higher pacing frequencies, as shown in neonatal rat ventricular myocytes in which I_{Ks} was overexpressed (39). • I_{K1}: Increases in both current density (27,40,41) and mRNA levels of I_{K1} (40) have been reported in human psAF. Increased I_{K1} causes a more negative RMP in psAF versus SR human atrial myocytes (31,40). • Na^+/Ca^{2+} exchange current (I_{NaCa}): Abnormal function and increased expression of the exchange protein have been reported in human psAF and in a sheep model of psAF (8,31,40,42,43). The increase in I_{NaCa} may be an adaptive response to cellular Ca^{2+} loading and helps to reduce the Ca^{2+} overload induced by rapid atrial pacing. Na^+ overload, which induces Ca^{2+} influx via the reverse-mode of the exchanger, has been implicated in Ca^{2+} overload and related arrhythmogenesis. Additionally, an increase in the forward-mode Ca^{2+} extrusion has been linked to delayed afterdepolarizations (DADs) [61, 124]. • RyR: In myocytes from AF hearts, leaky RyR channels can cause spontaneous Ca^{2+} release events known as Ca^{2+} sparks and Ca^{2+} waves, as reported in several studies (43–46). Remarkably, these events can occur despite unaltered sarcoplasmic reticulum Ca^{2+} content. • SERCA: Human psAF has been associated with a decrease in SERCA activity and reduced SERCA protein expression, which can explain the slower decay of [Ca^{2+}]i in psAF compared to SR (8,31).

In our model, psAF was simulated by modifying ionic conductances and Ca^{2+}-handling components according to experimental data. In the Courtemanche model, I_{to}, I_{CaL}, and I_{kur} conductances were reduced by 50%, 70%, and 50%, respectively, while I_{K1} conductance was doubled (47). These changes reproduce the APD shortening and enhanced repolarization stability typical of AF-remodeled atrial cells.

Modulators – ANS imbalance. The imbalance of the ANS represents an important pathophysiological mechanism for AF genesis and maintenance (48–50). Autonomic imbalance is not only a modulating factor of AF, but both the triggers and the substrate of the arrhythmia can be influenced by such an imbalance (51,52). Sympathetic stimulation (SS) affects atrial myocytes by activating the β-adrenergic signaling cascade, which triggers the phosphorylation of various cellular substrates by PKA. In the Courtemanche model, the effects of β-adrenergic stimulation were modeled as proposed by Gonzalez de la Fuente et al. (53). This involved modeling the increases in the maximal conductances of I_{CaL} and I_{Ks} and the decrease in the maximal conductance of Ito following the experimentally reported concentration-dependent conductance modulation curves. At an Iso concentration of 1 µM, the

maximal conductances of I_{CaL} and I_{Ks} were increased by 160.6% and 65.7%, respectively, while the maximal conductance of Ito was reduced by 18.6%. The parasympathetic stimulation (PSS) effects were described by introducing the ACh activated potassium current I_{KACh} in the models to account for the activation of G-protein activated inwardly rectifying potassium channels induced by ACh. The I_{KACh} formulation was based on the study by Kneller et al. (54) and subsequently updated as proposed by Bayer et al. (55).

The exact shape and structure of the neural network in the myocardium are not fully known, but some works have documented the presence of between 500 and 1500 ganglia of different sizes in the atrial and ventricular myocardium (56). These ganglia may contain 200 to 1000 neurons (56–58), including efferent neurons, afferent neurons and local interneurons that receive inputs from both efferent and afferent neurons. Although the vast majority of ganglion cells are cholinergic, most ganglia also contain adrenergic nerve fibers (59). The vast majority of these ganglia are organized into ganglionated plexi (GPs) on the surface of the atria and ventricles (57) and are more abundant epicardially than endocardially (60). Although their location, shape and size can vary, intrinsic cardiac ganglia are usually distributed at specific regions in many mammals, including humans (56,61,62). In particular, with regards to the atria, five major atrial GPs have been reported to be embedded in epicardial fat pads located near the PVs (56,57). They have been named based on clinical anatomy: the superior right atrial GP (SRA-GP), located on the posterior superior surface of the RA close to the junction of the SVC and RA; the superior left atrial GP (SLA-GP), located on the posterior surface of the LA between the PVs; the posterior right atrial GP (PRA-GP), located on the posterior surface of the RA adjacent to the inter atrial groove; the posteromedial left atrial GP (PMLA-GP), located on the posterior medial surface of the LA; and the posterolateral left atrial GP (PLLA-GP), located on the posterior lateral surface of the LA base on the atrial side of the atrio-ventricular groove.

Considering that the GPs shown predominance of parasympathetic activity, parasympathetic effects were incorporated by increasing the concentration of ACh in randomly distributed islands within the tissue. We defined 4 different 3D models corresponding to distinct spatial ACh release configurations throughout the atria. These models were based on different experimental and computational studies, resulting in two different percentages of ACh release sites (i.e., 8% and 30%).

•**O08: Octopus 8%.** The heterogeneous ACh release in the atria was realistically represented by modeling the GPs location following the anatomical study by Armour et al. (57), as represented in

Co-funded by the European Union

Figure 3. This model included the anatomical locations of the GPs plus the nerves departing from the GPs. Specifically, the five major GPs (SRA-GPs, SLA-GPs, PRA-GPs, PMLA-GPs and PLLA-GPs) were considered in this model. To additionally take into account the nerves communicating the GPs with the atrial tissue, we modeled the GPs following the octopus hypothesis (63). Considering that the neural cell distribution is mainly epicardial (59), we concentrated the ACh release mostly in the two more external layers, as represented in Figure 4. In the O08 model, considering both the GPs bodies and the nerves departing from them, 8% of all the mesh nodes were ACh release nodes. The model is represented in panel A) of Figure 5.

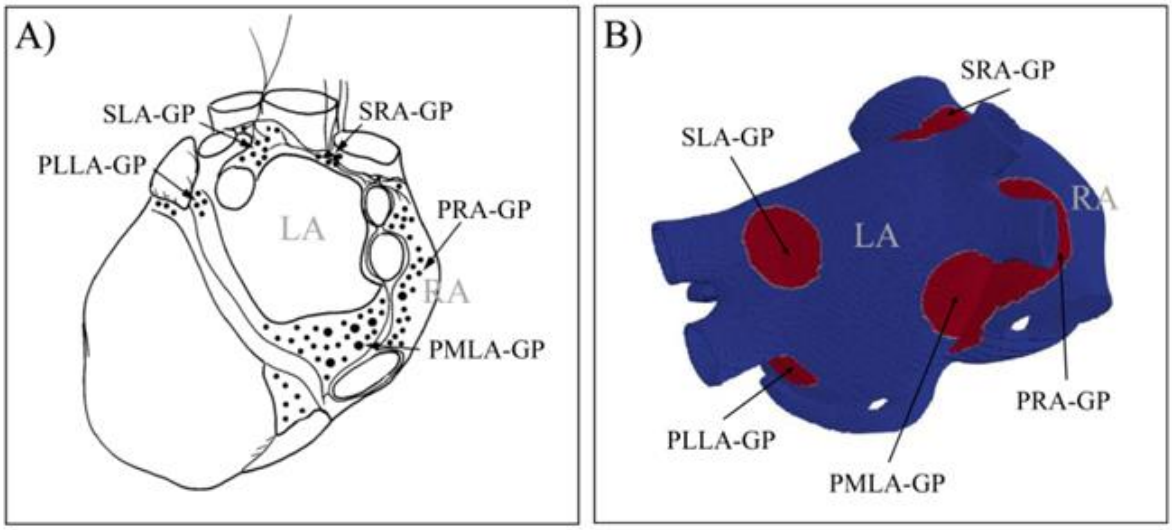

Figure 3: (A) anatomical description by Armour et al. [52]. (B) computational model used in this study, with GPs represented in red.

• **D08: Diffuse 8%.** To assess the impact of the spatial distribution of ACh release, we built another 3D model in which 8% of the nodes were uniformly randomly selected all over the atria to be ACh release nodes. This model is represented in Figure 5, panel B), and referred to as D08.

• **O30: Octopus 30%.** We defined another 3D model by introducing a new hypothesis: the existence of minor branches that extend from the GPs and main nerves (56,64). In this model, the GPs and nerves of the octopus configuration were identified as release nodes. Additional nodes all over the atria were

ERA4Health Partnership

Co-funded by the European Union

identified as release nodes with a probability that decreased with the distance to the octopus, completing a total of 30% of ACh release nodes in the atria. The model was consequently denoted as O30, and is represented in Figure 5, panel C).

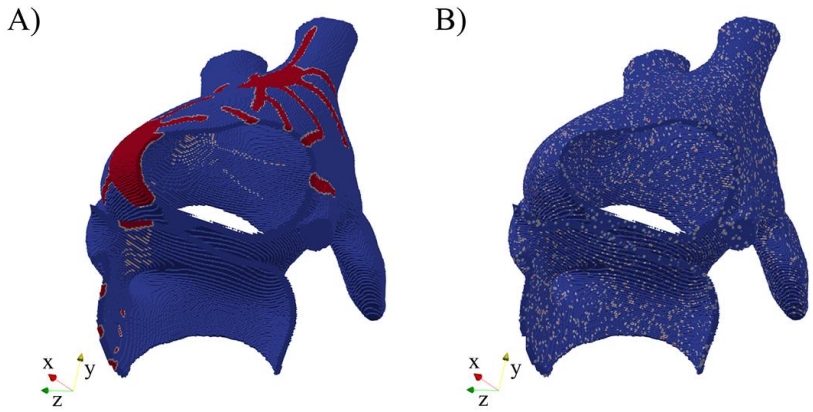

Figure 4: Sections of the left atrium for the O08 model (A) and D08 model (B). In the O08 the AChrelease nodes (red) are concentrated in the 2 most external layers of the mesh, while in the D08 model they are uniform randomly distributed in all the three node layers.

• **D30: Diffuse 30%.** In this model, 30% of all nodes in the atria were uniformly randomly selected as ACh release nodes. The D30 model is represented in Figure 5, panel D).

For each of the identified release nodes, ACh was simulated to cyclically vary in time following a sinusoidal waveform of frequency equal to 0.125 Hz. We tested different mean concentrations of ACh (ACh), equal to 0.05 and 0.075 µM, and different peak-to-peak variations of ACh (ΔACh), equal to 0, 0.05 and 0.1 µM. All simulated ACh values were within the physiological limits tested in preceding studies (0 0.1 µM) (55).

Stimuli. In the whole-atria models a S1-S2 protocol was used to initiate the arrhythmia, with the S1 stimulus delivered at a line joining the region between the superior and inferior left PVs and the region between the right PVs, and the S2 stimulus being subsequently applied parallel to the first one starting from the inferior left PV and covering only half of the S1 line length.

Co-funded by the European Union

Dominant frequency characterization. To characterize atrial activity both in clinical and simulated signals, two main parameters were computed: the dominant frequency (*ff)* and its modulation magnitude (*Δff*). The parameter *ff* represents the mean activation frequency of atrial electrical activity, providing an estimate of the average rate of fibrillatory waves. The parameter *Δff* quantifies the magnitude of frequency modulation over time, mainly reflecting respiration-related oscillations in atrial activation rate. These two metrics were consistently derived from both patient ECG recordings and model simulations, enabling direct comparison between clinical and in-silico dynamics.

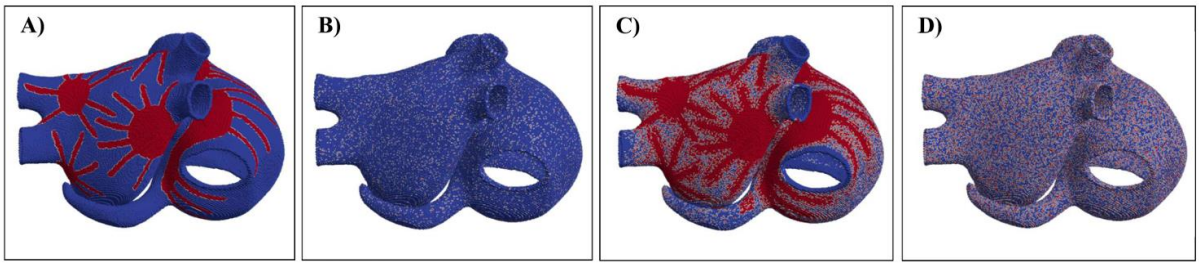

Figure 5: 3D biatrial anatomies, with ACh release nodes depicted in red. Representation of (A) O08 model, (B) D08 model, (C) O30 model and (D) D30 model.

Results. In the 3D biatrial models, S1-S2 stimulation was able to generate multiple stable rotors. The induced fibrillatory patterns were different for the distinct spatial configurations of ACh release, with the generation of 2 to 5 stable rotors, as represented in Figure 6. We observed a general increase in the number of stable rotors with the highest percentage of ACh release nodes (O30 and D30). In all cases, the rotors stabilized in the LA, with only four exceptions: O30 model and D30 with ACh varying from 0.0 to 0.1 µM, D30 model with ACh varying from 0.025 to 0.075 µM and D30 model with ACh equal to 0.05 µM, for which 2 to 4 stable rotors in the LA and 1 to 2 stable rotors in the RA were observed. For the four spatial ACh release models, i.e. O08, D08, O30 and D30, the atrial dominant frequency followed the induced ACh(n) patterns (Figure 7). For O08 and D08, the Pearson correlation coefficient values r were above 0.72 and 0.45 for ΔACh = 0.1 and ΔACh = 0.05 µM, respectively, while for O30 and D30, the r values were above 0.54 and 0.80. *Δff* was found to be highly dependent on ΔACh. Furthermore, for 30% ACh release nodes, *Δff* was higher in the diffuse than in the octopus configuration. For 8%, the spatial distribution of ACh release did not have significant effects on *Δff* when all other factors were kept constant. We observed that when the fibrillatory patterns in the 3D models were similar to one another, as occurs for the O08 and D08 models with ΔACh = 0.05 µM, or

Co-funded by the European Union

for the D08 model with ΔACh=0.0μM, *ff* was increasing with ACh. As expected, we also observed an increase in the dominant f-wave frequency with the number of stable rotors in the atria, regardless the ACh level.

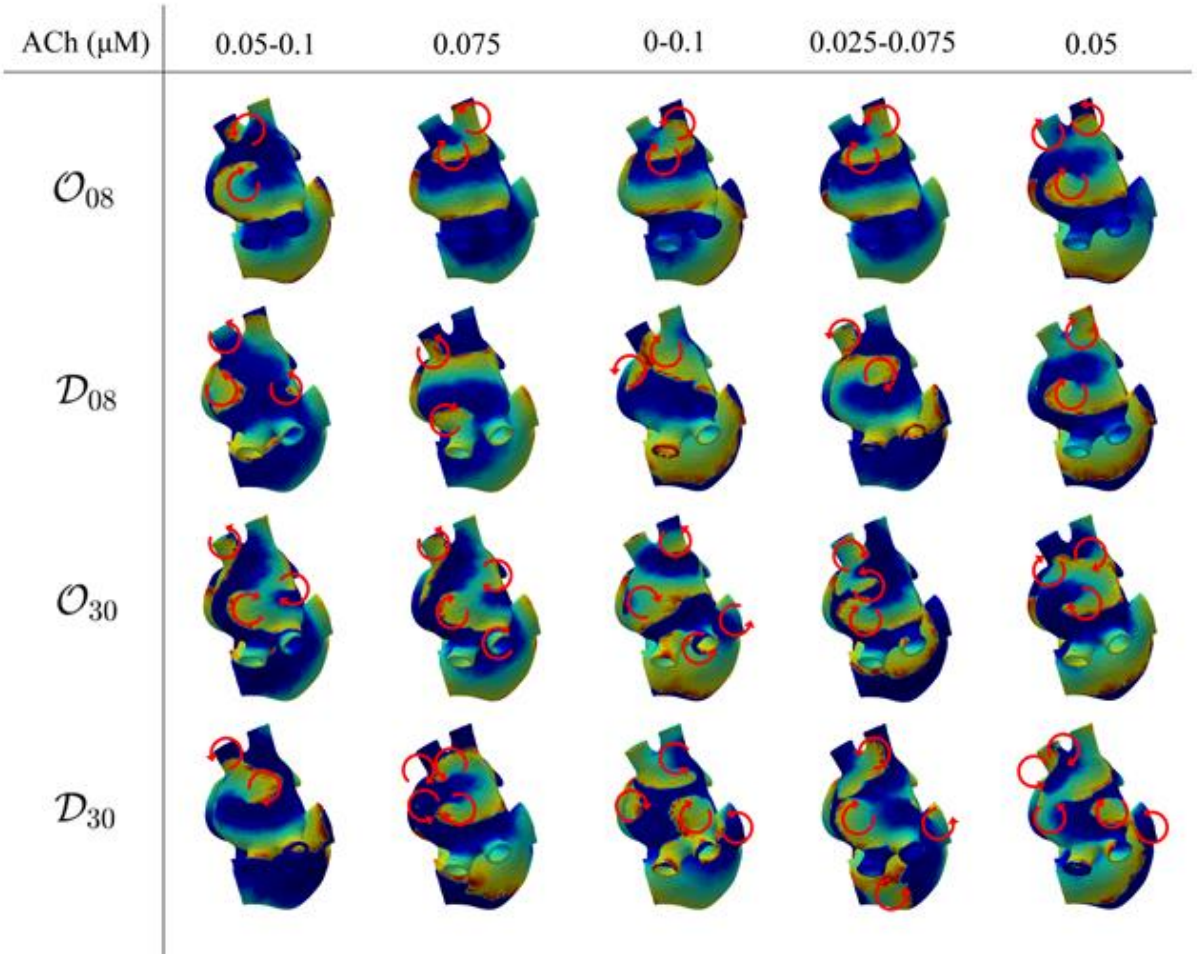

Figure 6: Voltage maps representative of the induced fibrillatory pattern after application of S1-S2 stimulation. Each circular arrow represents the location of a rotor with its direction of rotation. The Ach values indicate a constant ACh release when only a number is reported, corresponding to mean ACh, and to a range of variation when two numbers are given, corresponding to mean ACh ± ΔACh.

ERA4Health Partnership

Co-funded by
the European Union

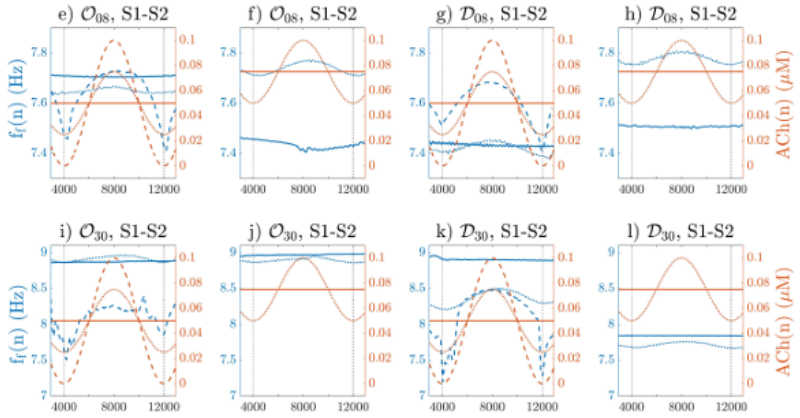

Figure 7: Results from 3D biatrial simulations with O08 and D08 (furst row, panels e, f, g, h) and O30 and D30 (second row, panels i, j, k, l) spatial configurations of ACh release and application of a S1-S2 protocol. ff(n) (blue) and ACh(n) (red) are plotted in all panels for ACh = 0.05 µM (a, c, e, g, i, k, m, o, q, s) and ACh = 0.075 µM(b, d, f, h, j, l, n, p, r, t). Solid/dotted/dashed lines represent ΔACh values of 0.0/0.05/0.1 µM . In panels (b, d), ΔACh=0.1 µM was not included, as ACh(n) contained non-physiological ACh values

The octopus O and diffuse D configurations did not seem to correlate to the induced fibrillatory pattern and did not cause significant variations in terms of ff, at least for 8% ACh release nodes. For 30% ACh release nodes, significant differences in *ff* could be observed in several cases (up to-12.5% when comparing O30 with respect to D30 under ACh=0.075 µM and ΔACh=0 µM) while little or no differences could be observed in other cases. Also in this case, we observed a non-monotonic dependence between *ff* and ΔACh. Similarly, both the minimum ACh and ΔACh can potentially influence *ff*, but determining the extent of their impact is further complicated by the presence of different fibrillation patterns.

3 Planned Work: Investigating the Role of the Epicardial Adipose Tissue Secretome in Atrial Fibrillation Vulnerability

Among the many risk factors for AF, obesity has been identified as an independent contributor, with epicardial adipose tissue (EAT) emerging as a stronger predictor of AF risk than body mass index (BMI)

ERA4Health
Partnership

Co-funded by the European Union

(65). EAT is a specialized fat depot located between the myocardium and pericardium, and its pro-arrhythmic effects are of particular interest for understanding the substrate underlying AF.

EAT has been shown to affect AF in two major ways (65):

1. Electrical Mechanisms: EAT influences ion channel function, calcium handling, and GJ integrity, leading to the promotion of ectopic beats and re-entrant circuits, which are key drivers of AF.
2. Structural Mechanisms: EAT releases inflammatory molecules that promote fibrosis, leading to slow and heterogeneous conduction, and can infiltrate the atrial myocardium, disturbing normal electrical conduction. Additionally, EAT impacts the autonomic nervous system (ANS) in the heart, further contributing to arrhythmic susceptibility.

Given these mechanisms, targeting EAT-mediated inflammation, fibrosis, and autonomic modulation may provide therapeutic opportunities for reducing the burden of AF.

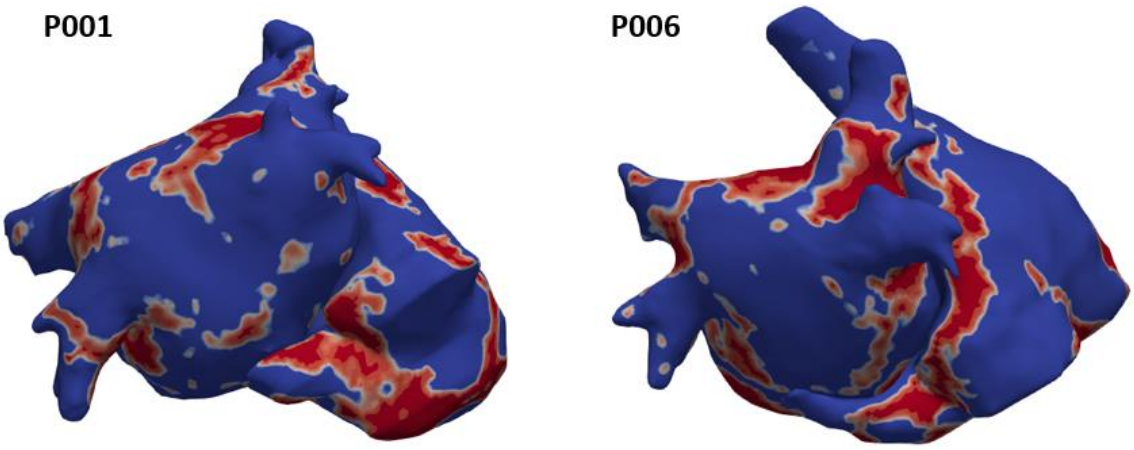

Figure 8: Patient-specific epicardial fat projection on the surface of the LA and RA.

The Window of Vulnerability (WoV) and the Role of EAT Secretome. To better understand the influence of EAT on AF, it is essential to explore how the distribution and secretome of EAT affect the window of vulnerability (WoV) in the atrial substrate. The WoV refers to the range of coupling intervals of a premature atrial stimulus (S2) that can successfully induce sustained AF. In an experimental setting, the WoV is assessed by delivering a train of regular stimuli (S1) to establish steady-state atrial activation, followed by a premature extra-stimulus (S2) introduced at progressively shorter coupling intervals. The outcome is recorded in terms of whether the S2 fails to capture, induces a short ectopic

beat, or triggers sustained AF (lasting more than 1-2 seconds or more than 10 cycles, depending on the protocol).

To evaluate the impact of the EAT secretome on AF vulnerability, we propose the following experimental approach:

Approach:

1. Define EAT Regions: Develop average atrial fat maps to identify the distribution of EAT across different individuals, based on the maps represented in Figure 8. Using these maps, create patient subgroups based on the percentage of EAT and atrial surface coverage.
2. Set Transmural Levels: Model the electrophysiological effects of EAT at three different transmural levels—epicardial, mid-myocardial, and endocardial. This will allow us to assess how the penetration of EAT influences atrial conduction and AF susceptibility (66).
3. Simulation Implementation: Using the ELVIRA(6) simulation platform, assign EAT regions and associated electrophysiological parameters to the atrial models.
4. Run Simulations: Apply the standard S1-S2 protocol at key atrial sites to compute the WoV for each model, focusing on how variations in EAT distribution and transmural depth influence AF induction.
5. Analysis: Compare the width of the WoV, changes in conduction velocity, and AF susceptibility across subgroups and transmural depths.

Expected Outcome. This study will quantify the impact of both the amount and transmural penetration of EAT on AF vulnerability. By analysing the interplay between EAT distribution, secretome composition, and AF substrate properties, we aim to identify critical factors that contribute to AF initiation and maintenance. Ultimately, these insights could guide the development of targeted therapies aimed at mitigating the adverse effects of EAT in AF patients.

4 Personalized Atrial Models for Substrate Characterization

Alongside the development of a generic atrial electrophysiological framework, we worked at the personalization of the computational models to reproduce patient-specific atrial conduction patterns. This effort is crucial for bridging the gap between mechanistic simulations and clinical observations, allowing the model to be used as a tool to interpret patient data and to investigate the underlying arrhythmic substrate.

Co-funded by the European Union

Clinical context and data acquisition. The personalization pipeline was developed with data provided by the University Hospital Puerta del Mar (Cádiz, Spain), which is conducting a prospective clinical study on patients with symptomatic persistent AF referred for de novo ablation. All patients underwent high-resolution multidetector CT (MDCT) scans before the procedure to reconstruct the LA anatomy and wall thickness. Electroanatomical mapping was then performed with the CARTO3 system using a high-density PentaRay catheter. Mapping was carried out in three conditions: during AF, during SR, and during a triple-extrastimulus (TE) pacing protocol delivered from the distal coronary sinus. The extrastimuli were delivered at progressively shorter coupling intervals relative to the atrial effective refractory period (AERP), a protocol designed to unmask hidden slow-conduction (HSC) regions that may not be apparent in SR mapping.

For each mapping condition, bipolar electrograms (EGMs) were recorded, annotated, and quality-checked. Local activation times (LATs) were defined as the time of the steepest deflection in bipolar EGMs during activation. Voltage maps were derived from the peak-to-peak amplitude of bipolar EGMs. These multimodal data were used as reference targets for model calibration and validation.

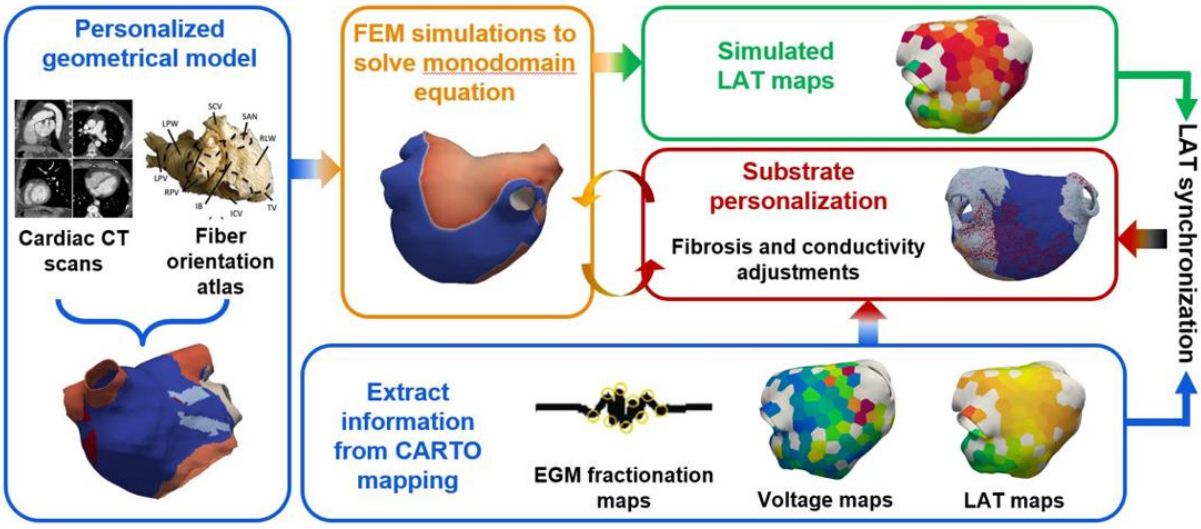

Figure 9: Pipeline for model personalization.

Personalization workflow. The pipeline therefore combined multiple data sources—CT-derived anatomy, clinical LATs and voltage maps—to iteratively refine the simulated substrate, progressively improving its fidelity to the clinical observations (Figure 9). A total of four patients were analyzed up to now. Patient-specific LA anatomies were segmented from MDCT scans using the ADAS software,

Co-funded by the European Union

which also provided estimates of regional wall thickness. The segmented volume was meshed into a high-resolution tetrahedral grid with an average edge length of approximately 350 µm, resulting in a number of nodes and elements summarized in Figure 10.

The LA geometry was divided into five anatomical regions in which regional fiber orientations were assigned according to the atlas described by Ferrer et al (3). Electrophysiological properties were assigned according to atrial region: the tissue was subdivided into four functional regions, each represented by a regionally adapted version of the electrically remodeled Courtemanche model. Distinct model variants were defined for the LA wall, the LAA, PVs, BB, and the MVR, incorporating region-specific adjustments of ionic conductances. This setup allowed the integration of both anatomical and functional variability in the atrial substrate.

The monodomain equation was solved using the in-house finite-element software ELVIRA(6), enabling the simulation of three-dimensional wavefront propagation throughout the atrial geometry. Prior to stimulation, single-cell models were paced at a cycle length of 800 ms for 16 minutes to reach a steady state, and the resulting states were used to initialize the tissue simulations. Since only the LA was modeled, stimuli were applied in the region corresponding to the earliest activation identified in the clinical LAT maps. Additional pacing protocols reproduced the clinical TE protocol to mimic the same conditions under which clinical recordings were acquired.

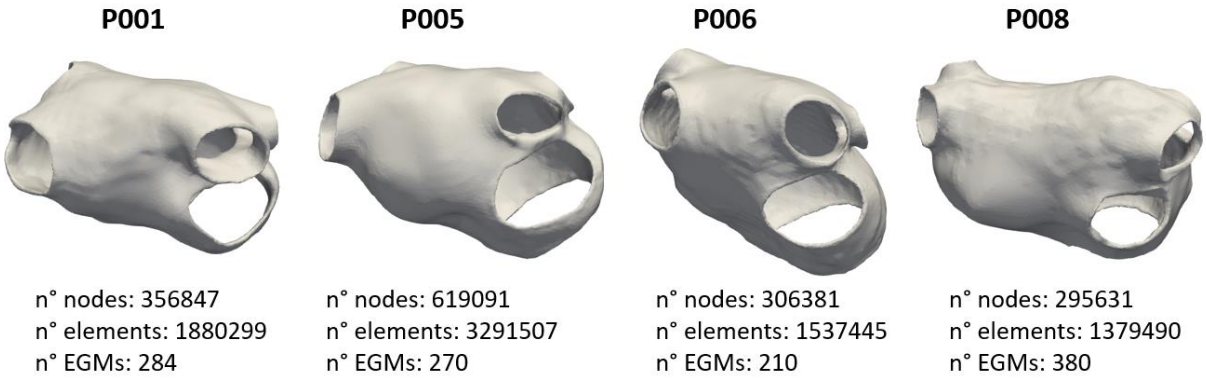

Figure 10: Mesh visualization and description for the 4 analyzed patients.

For each patient, clinical EGMs were acquired using the CARTO system, with the number of available recordings ranging from 210 to 380. From these recordings, four LAT and voltage maps were computed per patient: one corresponding to SR—considering the last sinus beat prior to the TE protocol—and three corresponding to the individual extrastimuli of the TE protocol. Since the computational model

Co-funded by
the European Union

represents only the LA, sinus activation was reproduced by applying a stimulus in the region corresponding to the earliest activation site identified from the clinical SR LAT map. For the TE protocol simulations, stimuli were applied at locations corresponding to the mean position of the stimulation catheter tip, as determined from the CARTO data.

Fibrosis was incorporated based on the voltage map obtained from the last sinus beat preceding the TE protocol. Two regions were identified according to bipolar EGM amplitude: **dense fibrosis** (amplitude < 0.2 mV) and **border zone** areas (0.2–0.5 mV). Within these regions, 20% and 10% of mesh nodes, respectively, were assigned fibroblast properties following the active fibroblast model by MacCannell et al (25), as represented in Figure 11.

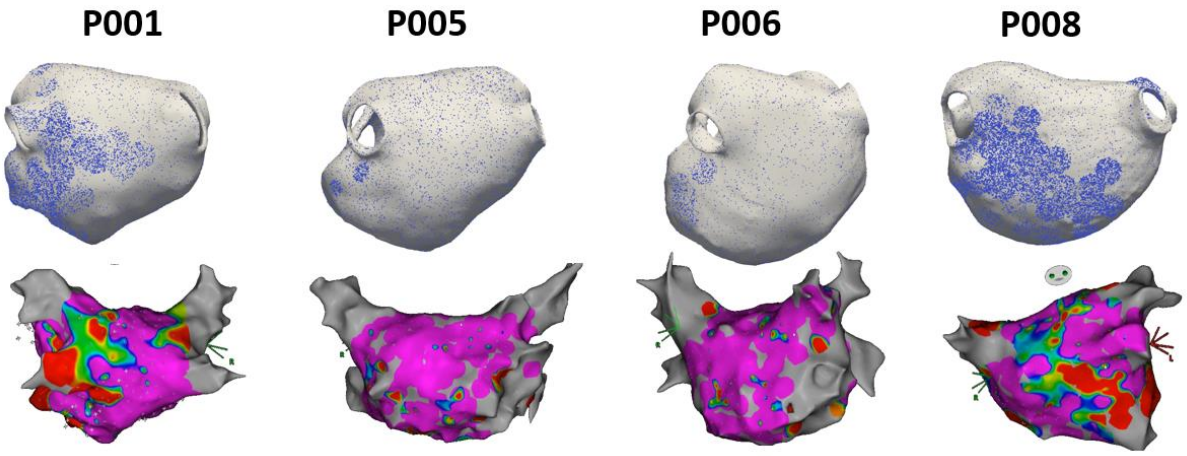

Figure 11: generated fibrotic maps (first row) compared with the CARTO voltage maps for the same patients (second row).

Finally, simulated unipolar EGMs were computed by placing virtual electrodes at the same coordinates as those recorded in the CARTO system. To ensure realistic electrode–tissue spacing, the electrode positions were slightly shifted along the normal direction of the atrial surface by approximately 5 mm.

Preliminary results and insights. The application of the personalized modeling pipeline to the four available patients demonstrated the ability of the framework to reproduce clinically observed activation patterns during both SR and the TE protocol. Figure 12 shows the clinical LAT maps for the first, second, and third extrastimuli, from both anterior and posterior atrial views. In particular, patients 1 and 5 clearly exhibited progressive LAT prolongation with the second and third extrastimuli, revealing areas of slow conduction that emerged under fast pacing conditions.

ERA4Health
Partnership

Co-funded by
the European Union

For each patient, four sets of simulations were performed to systematically assess the impact of structural and electrophysiological substrate properties. The tested configurations included:

1. a **baseline model** without fibrosis,
2. a **fibrotic model**,
3. a **fibrotic model with reduced conductances**, and
4. a **fibrotic model with increased conductances**.

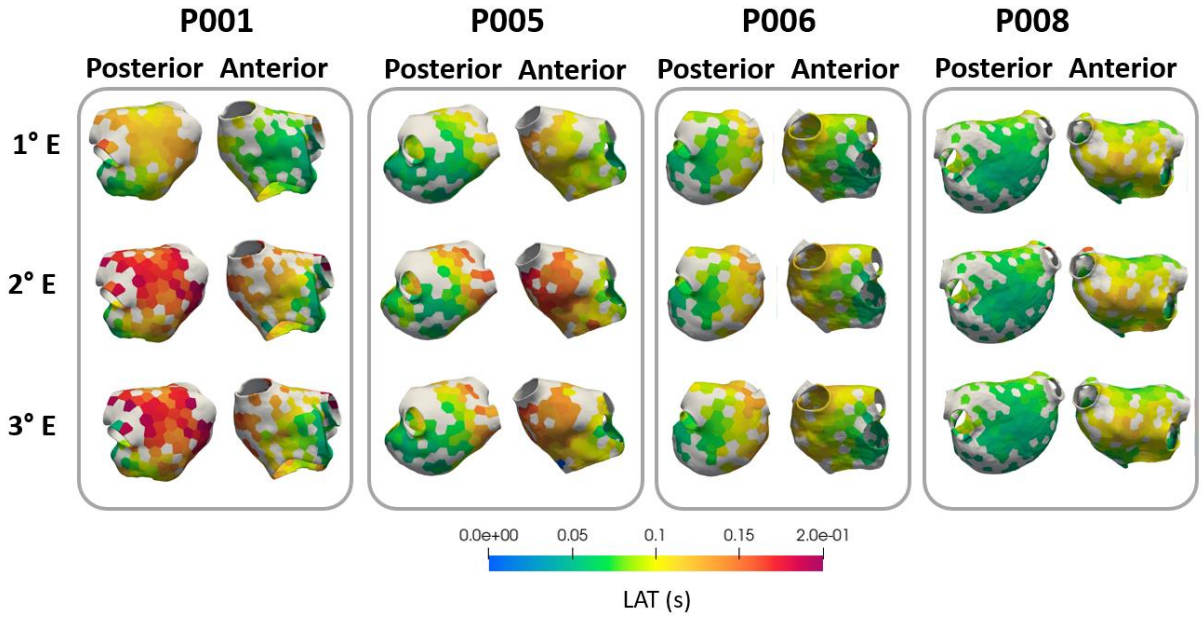

Figure 12: LAT maps (posterior and anterior views) computed from the clinical signals for the four different patients. The first row represents LAT maps for the first extrastimulus (1°E), the second row represents LAT maps for the second extrastimulus (2°E) and third row represents LAT maps for the third extrastimulus (3°E).

The agreement between simulated and clinical LATs was quantified using different metrics, summarized in Figure 13:

- the **Pearson correlation coefficient (r)**, evaluating linear agreement;
- the **concordance correlation coefficient (ρc)**, which accounts for both accuracy and precision;
- The **median (M) of the computed error** between clinical and simulated LAT maps;
- The **mean (m) of the computed error** between clinical and simulated LAT maps;
- The **standard deviation (SD) of the computed error** between clinical and simulated LAT maps;

ERA4Health
Partnership

Co-funded by the European Union

Across all patients, a gradual decline in both *r* and *ρc* values was observed from LAT1 to LAT3, reflecting the increasing complexity of conduction dynamics under rapid pacing. Outliers were excluded from the analysis to emphasize the main agreement trends. The cross-patient summary of all metrics confirmed that introducing fibrosis or modulating conductances primarily affected the overall offset (mean and median) and, consequently, the concordance coefficient, while the SD remained largely unchanged. The best-performing configurations for each patient and metric are highlighted in red in Figure 13: higher *r* and *ρc* values indicate stronger agreement, whereas mean and median values closer to zero and smaller SDs reflect improved accuracy and reduced variability. Although no single model variant consistently outperformed the others across all patients, cases 6 and 8 showed better metric stability and reduced variability between the first and third extrastimuli, suggesting a less heterogeneous and structurally simpler substrate.

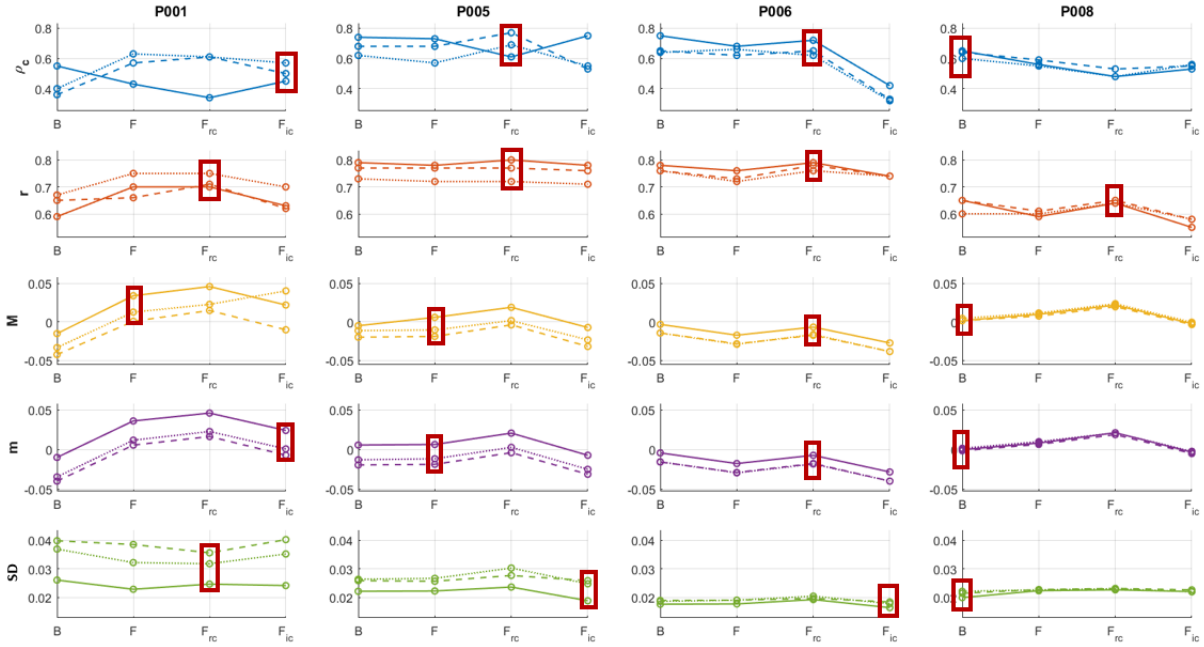

Figure 13: Cross-patient summary of all metrics. First row: concordance correlation coefficient (ρc). Second row: Pearson correlation coefficient (r); third row: median (M) of the computed error between clinical and simulated LAT maps; forth row: mean (m) of the computed error between clinical and simulated LAT maps; fifth row: standard deviation (SD) of the computed error between clinical and simulated LAT maps. Continuos/dashed/dotted lines represent the 1st, 2nd, and 3dh estrastimulus, respectively.

ERA4Health Partnership

Overall, these results confirm that the inclusion of fibrosis enhances physiological realism and improves agreement with clinical LAT maps, particularly for later extrastimuli that are more sensitive to conduction-slowing features. However, discrepancies between stimulation cases highlight the need for further personalization of restitution properties—such as effective refractory periods (ERPs)—to fully capture patient-specific conduction dynamics. Future developments will focus on refining these aspects to uncover the mechanistic basis of the observed patient responses and to enhance the predictive power of the model.

5 Discussion and future work

The multiscale in-silico model developed in this work package represents a powerful tool to explore the electrical behavior of the atria under both physiological and pathological conditions. Its main strength lies in the mechanistic nature of the approach: by linking cellular electrophysiology to three-dimensional atrial anatomy and regional tissue properties, the model allows us to test specific hypotheses on how structural remodelling, ionic alterations, and autonomic influences interact to shape conduction patterns. This level of detail is crucial for identifying mechanisms that sustain atrial fibrillation and for interpreting how different substrate features—such as fibrosis or altered ionic conductances—affect the formation of regions of slow or discontinuous conduction.

This framework can also be adapted to reproduce patient-specific atrial geometries and electrophysiological properties. This capability will be exploited to simulate the propagation maps recorded in patients enrolled in the project, thereby enabling the comparison of simulated and observed activation sequences. Such personalized simulations are expected to shed light on the mechanistic origin of patient-specific conduction abnormalities and help disentangle the contributions of structural versus functional remodeling to the arrhythmic substrate.

Despite these strengths, the model has some limitations. While it incorporates realistic anatomy and detailed ionic dynamics, certain structural features—such as microscopic fibrosis patterns, heterogeneous gap-junction distribution, or anisotropic collagen deposition—are simplified or represented indirectly

Future efforts within the project will focus on addressing these challenges by integrating additional patient-specific information, refining fibrosis characterization, and systematically validating model

predictions against the clinical datasets collected in WP1 and WP5. By iteratively improving the model in this way, we aim to build a robust in-silico platform capable of reproducing individual patient activation maps and providing mechanistic insights into the arrhythmic substrate. Ultimately, these simulations will help explain why certain regions act as drivers or barriers to conduction and how ablation strategies might be optimized—alone or in combination with pharmacological treatment—to target the specific substrate present in each patient.

6 References

1. Courtemanche M, Ramirez RJ, Nattel S. Ionic mechanisms underlying human atrial action potential properties: insights from a mathematical model. Am J Physiol-Heart Circ Physiol. 1 luglio 1998;275(1):H301–21.

2. Yue L, Feng J, Gaspo R, Li GR, Wang Z, Nattel S. Ionic Remodeling Underlying Action Potential Changes in a Canine Model of Atrial Fibrillation. Circ Res. ottobre 1997;81(4):512–25.

3. Ferrer A, Sebastián R, Sánchez-Quintana D, Rodríguez JF, Godoy EJ, Martínez L, et al. Detailed Anatomical and Electrophysiological Models of Human Atria and Torso for the Simulation of Atrial Activation. PloS One. 2015;10(11):e0141573.

4. Seemann G, Höper C, Sachse FB, Dössel O, Holden AV, Zhang H. Heterogeneous three-dimensional anatomical and electrophysiological model of human atria. Philos Transact A Math Phys Eng Sci. 15 giugno 2006;364(1843):1465–81.

5. Wesselink R, Neefs J, van den Berg NWE, Meulendijks ER, Terpstra MM, Kawasaki M, et al. Does left atrial epicardial conduction time reflect atrial fibrosis and the risk of atrial fibrillation recurrence after thoracoscopic ablation? Post hoc analysis of the AFACT trial. BMJ Open. 9 marzo 2022;12(3):e056829.

6. Heidenreich EA, Ferrero JM, Doblaré M, Rodríguez JF. Adaptive macro finite elements for the numerical solution of monodomain equations in cardiac electrophysiology. Ann Biomed Eng. luglio 2010;38(7):2331–45.

7. Sanders P, Morton JB, Davidson NC, Spence SJ, Vohra JK, Sparks PB, et al. Electrical remodeling of the atria in congestive heart failure: electrophysiological and electroanatomic mapping in humans. Circulation. 23 settembre 2003;108(12):1461–8.

8. Heijman J, Voigt N, Nattel S, Dobrev D. Cellular and molecular electrophysiology of atrial fibrillation initiation, maintenance, and progression. Circ Res. 25 aprile 2014;114(9):1483–99.

9. Allessie M. Electrical, contractile and structural remodeling during atrial fibrillation. Cardiovasc Res. maggio 2002;54(2):230–46.

10. Heijman J, Algalarrondo V, Voigt N, Melka J, Wehrens XHT, Dobrev D, et al. The value of basic research insights into atrial fibrillation mechanisms as a guide to therapeutic innovation: a critical analysis. Cardiovasc Res. 1 aprile 2016;109(4):467–79.

11. Platonov PG, Mitrofanova LB, Orshanskaya V, Ho SY. Structural abnormalities in atrial walls are associated with presence and persistency of atrial fibrillation but not with age. J Am Coll Cardiol. 15 novembre 2011;58(21):2225–32.

12. Kostin S, Klein G, Szalay Z, Hein S, Bauer EP, Schaper J. Structural correlate of atrial fibrillation in human patients. Cardiovasc Res. 1 maggio 2002;54(2):361–79.

13. Burstein Brett, Comtois Philippe, Michael Georghia, Nishida Kunihiro, Villeneuve Louis, Yeh Yung-Hsin, et al. Changes in Connexin Expression and the Atrial Fibrillation Substrate in Congestive Heart Failure. Circ Res. 4 dicembre 2009;105(12):1213–22.

14. Rohr S. Myofibroblasts in diseased hearts: new players in cardiac arrhythmias? Heart Rhythm. giugno 2009;6(6):848–56.

15. Shiraishi I, Takamatsu T, Minamikawa T, Onouchi Z, Fujita S. Quantitative histological analysis of the human sinoatrial node during growth and aging. Circulation. giugno 1992;85(6):2176–84.

16. Camelliti P, Devlin GP, Matthews KG, Kohl P, Green CR. Spatially and temporally distinct expression of fibroblast connexins after sheep ventricular infarction. Cardiovasc Res. 1 maggio 2004;62(2):415–25.

17. Kohl P, Camelliti P, Burton FL, Smith GL. Electrical coupling of fibroblasts and myocytes: relevance for cardiac propagation. J Electrocardiol. ottobre 2005;38(4 Suppl):45–50.

18. Tanaka K, Zlochiver S, Vikstrom KL, Yamazaki M, Moreno J, Klos M, et al. Spatial distribution of fibrosis governs fibrillation wave dynamics in the posterior left atrium during heart failure. Circ Res. 12 ottobre 2007;101(8):839–47.

Co-funded by
the European Union

19. Miragoli M, Salvarani N, Rohr S. Myofibroblasts induce ectopic activity in cardiac tissue. Circ Res. 12 ottobre 2007;101(8):755–8.

20. Pedrotty DM, Klinger RY, Kirkton RD, Bursac N. Cardiac fibroblast paracrine factors alter impulse conduction and ion channel expression of neonatal rat cardiomyocytes. Cardiovasc Res. 1 settembre 2009;83(4):688–97.

21. Trayanova NA. Mathematical approaches to understanding and imaging atrial fibrillation: significance for mechanisms and management. Circ Res. 25 aprile 2014;114(9):1516–31.

22. Jacquemet V, Henriquez CS. Loading effect of fibroblast-myocyte coupling on resting potential, impulse propagation, and repolarization: insights from a microstructure model. Am J Physiol Heart Circ Physiol. maggio 2008;294(5):H2040-2052.

23. Krueger MW, Rhode KS, O'Neill MD, Rinaldi CA, Gill J, Razavi R, et al. Patient-specific modeling of atrial fibrosis increases the accuracy of sinus rhythm simulations and may explain maintenance of atrial fibrillation. J Electrocardiol. 2014;47(3):324–8.

24. McDowell KS, Vadakkumpadan F, Blake R, Blauer J, Plank G, Macleod RS, et al. Mechanistic inquiry into the role of tissue remodeling in fibrotic lesions in human atrial fibrillation. Biophys J. 18 giugno 2013;104(12):2764–73.

25. Andrew MacCannell K, Bazzazi H, Chilton L, Shibukawa Y, Clark RB, Giles WR. A Mathematical Model of Electrotonic Interactions between Ventricular Myocytes and Fibroblasts. Biophys J. giugno 2007;92(11):4121–32.

26. Bernardi L, Keller F, Sanders M, Reddy PS, Griffith B, Meno F, et al. Respiratory sinus arrhythmia in the denervated human heart. J Appl Physiol Bethesda Md 1985. ottobre 1989;67(4):1447–55.

27. Van Wagoner DR, Pond AL, Lamorgese M, Rossie SS, McCarthy PM, Nerbonne JM. Atrial L-type Ca2+ currents and human atrial fibrillation. Circ Res. 3 settembre 1999;85(5):428–36.

28. Workman AJ, Kane KA, Rankin AC. The contribution of ionic currents to changes in refractoriness of human atrial myocytes associated with chronic atrial fibrillation. Cardiovasc Res. novembre 2001;52(2):226–35.

29. Boutjdir M, Le Heuzey JY, Lavergne T, Chauvaud S, Guize L, Carpentier A, et al. Inhomogeneity of cellular refractoriness in human atrium: factor of arrhythmia? Pacing Clin Electrophysiol PACE. novembre 1986;9(6):1095–100.

ERA4Health
Partnership

30. Bosch RF, Zeng X, Grammer JB, Popovic K, Mewis C, Kühlkamp V. Ionic mechanisms of electrical remodeling in human atrial fibrillation. Cardiovasc Res. ottobre 1999;44(1):121–31.

31. Grandi E, Pandit SV, Voigt N, Workman AJ, Dobrev D, Jalife J, et al. Human atrial action potential and Ca2+ model: sinus rhythm and chronic atrial fibrillation. Circ Res. 14 ottobre 2011;109(9):1055–66.

32. Sossalla S, Kallmeyer B, Wagner S, Mazur M, Maurer U, Toischer K, et al. Altered Na(+) currents in atrial fibrillation effects of ranolazine on arrhythmias and contractility in human atrial myocardium. J Am Coll Cardiol. 25 maggio 2010;55(21):2330–42.

33. Caballero R, de la Fuente MG, Gómez R, Barana A, Amorós I, Dolz-Gaitón P, et al. In humans, chronic atrial fibrillation decreases the transient outward current and ultrarapid component of the delayed rectifier current differentially on each atria and increases the slow component of the delayed rectifier current in both. J Am Coll Cardiol. 25 maggio 2010;55(21):2346–54.

34. Van Wagoner DR, Pond AL, McCarthy PM, Trimmer JS, Nerbonne JM. Outward K+ current densities and Kv1.5 expression are reduced in chronic human atrial fibrillation. Circ Res. giugno 1997;80(6):772–81.

35. Grammer JB, Bosch RF, Kühlkamp V, Seipel L. Molecular remodeling of Kv4.3 potassium channels in human atrial fibrillation. J Cardiovasc Electrophysiol. giugno 2000;11(6):626–33.

36. Brandt MC, Priebe L, Böhle T, Südkamp M, Beuckelmann DJ. The ultrarapid and the transient outward K(+) current in human atrial fibrillation. Their possible role in postoperative atrial fibrillation. J Mol Cell Cardiol. ottobre 2000;32(10):1885–96.

37. Brundel BJ, Van Gelder IC, Henning RH, Tuinenburg AE, Wietses M, Grandjean JG, et al. Alterations in potassium channel gene expression in atria of patients with persistent and paroxysmal atrial fibrillation: differential regulation of protein and mRNA levels for K+ channels. J Am Coll Cardiol. 1 marzo 2001;37(3):926–32.

38. Christ T, Wettwer E, Voigt N, Hála O, Radicke S, Matschke K, et al. Pathology-specific effects of the IKur/Ito/IK,ACh blocker AVE0118 on ion channels in human chronic atrial fibrillation. Br J Pharmacol. agosto 2008;154(8):1619–30.

39. Muñoz V, Grzeda KR, Desplantez T, Pandit SV, Mironov S, Taffet SM, et al. Adenoviral expression of IKs contributes to wavebreak and fibrillatory conduction in neonatal rat ventricular cardiomyocyte monolayers. Circ Res. 31 agosto 2007;101(5):475–83.

Co-funded by
the European Union

40. Dobrev D, Graf E, Wettwer E, Himmel HM, Hála O, Doerfel C, et al. Molecular basis of downregulation of G-protein-coupled inward rectifying K(+) current (I(K,ACh) in chronic human atrial fibrillation: decrease in GIRK4 mRNA correlates with reduced I(K,ACh) and muscarinic receptor-mediated shortening of action potentials. Circulation. 20 novembre 2001;104(21):2551–7.

41. Voigt N, Trausch A, Knaut M, Matschke K, Varró A, Van Wagoner DR, et al. Left-to-right atrial inward rectifier potassium current gradients in patients with paroxysmal versus chronic atrial fibrillation. Circ Arrhythm Electrophysiol. ottobre 2010;3(5):472–80.

42. Wang Y, Xu H, Kumar R, Tipparaju SM, Wagner MB, Joyner RW. Differences in transient outward current properties between neonatal and adult human atrial myocytes. J Mol Cell Cardiol. settembre 2003;35(9):1083–92.

43. Voigt N, Li N, Wang Q, Wang W, Trafford AW, Abu-Taha I, et al. Enhanced sarcoplasmic reticulum Ca2+ leak and increased Na+-Ca2+ exchanger function underlie delayed afterdepolarizations in patients with chronic atrial fibrillation. Circulation. 1 maggio 2012;125(17):2059–70.

44. Neef S, Dybkova N, Sossalla S, Ort KR, Fluschnik N, Neumann K, et al. CaMKII-dependent diastolic SR Ca2+ leak and elevated diastolic Ca2+ levels in right atrial myocardium of patients with atrial fibrillation. Circ Res. 2 aprile 2010;106(6):1134–44.

45. Greiser M, Kerfant BG, Williams GSB, Voigt N, Harks E, Dibb KM, et al. Tachycardia-induced silencing of subcellular Ca2+ signaling in atrial myocytes. J Clin Invest. novembre 2014;124(11):4759–72.

46. Chelu MG, Sarma S, Sood S, Wang S, van Oort RJ, Skapura DG, et al. Calmodulin kinase II-mediated sarcoplasmic reticulum Ca2+ leak promotes atrial fibrillation in mice. J Clin Invest. luglio 2009;119(7):1940–51.

47. Courtemanche M. Ionic targets for drug therapy and atrial fibrillation-induced electrical remodeling: insights from a mathematical model. Cardiovasc Res. maggio 1999;42(2):477–89.

48. Coumel P. Autonomic influences in atrial tachyarrhythmias. J Cardiovasc Electrophysiol. ottobre 1996;7(10):999–1007.

49. Coumel P. Cardiac arrhythmias and the autonomic nervous system. J Cardiovasc Electrophysiol. giugno 1993;4(3):338–55.

ERA4Health
Partnership

50. Bettoni M, Zimmermann M. Autonomic Tone Variations Before the Onset of Paroxysmal Atrial Fibrillation. Circulation. 11 giugno 2002;105(23):2753–9.

51. Scridon A, Şerban RC, Chevalier P. Atrial fibrillation: Neurogenic or myogenic? Arch Cardiovasc Dis. gennaio 2018;111(1):59–69.

52. Jons C, Raatikainen P, Gang UJ, Huikuri HV, Joergensen RM, Johannesen A, et al. Autonomic dysfunction and new-onset atrial fibrillation in patients with left ventricular systolic dysfunction after acute myocardial infarction: a CARISMA substudy. J Cardiovasc Electrophysiol. settembre 2010;21(9):983–90.

53. González de la Fuente M, Barana A, Gómez R, Amorós I, Dolz-Gaitón P, Sacristán S, et al. Chronic atrial fibrillation up-regulates β1-Adrenoceptors affecting repolarizing currents and action potential duration. Cardiovasc Res. 1 febbraio 2013;97(2):379–88.

54. Kneller J, Kalifa J, Zou R, Zaitsev AV, Warren M, Berenfeld O, et al. Mechanisms of atrial fibrillation termination by pure sodium channel blockade in an ionically-realistic mathematical model. Circ Res. 18 marzo 2005;96(5):e35-47.

55. Bayer JD, Boukens BJ, Krul SPJ, Roney CH, Driessen AHG, Berger WR, et al. Acetylcholine Delays Atrial Activation to Facilitate Atrial Fibrillation. Front Physiol. 4 settembre 2019;10:1105.

56. Pauza DH, Skripka V, Pauziene N, Stropus R. Morphology, distribution, and variability of the epicardiac neural ganglionated subplexuses in the human heart. Anat Rec. 1 agosto 2000;259(4):353–82.

57. Armour JA. The little brain on the heart. Cleve Clin J Med. febbraio 2007;74 Suppl 1:S48-51.

58. Choi EK, Zhao Y, Everett TH, Chen PS. Ganglionated plexi as neuromodulation targets for atrial fibrillation. J Cardiovasc Electrophysiol. dicembre 2017;28(12):1485–91.

59. Tan AY, Li H, Wachsmann-Hogiu S, Chen LS, Chen PS, Fishbein MC. Autonomic Innervation and Segmental Muscular Disconnections at the Human Pulmonary Vein-Atrial Junction. J Am Coll Cardiol. luglio 2006;48(1):132–43.

60. Chevalier P, Tabib A, Meyronnet D, Chalabreysse L, Restier L, Ludman V, et al. Quantitative study of nerves of the human left atrium. Heart Rhythm. maggio 2005;2(5):518–22.

61. Arora RC, Waldmann M, Hopkins DA, Armour JA. Porcine intrinsic cardiac ganglia. Anat Rec A Discov Mol Cell Evol Biol. marzo 2003;271(1):249–58.

62. Batulevicius D, Skripka V, Pauziene N, Pauza DH. Topography of the porcine epicardiac nerve plexus as revealed by histochemistry for acetylcholinesterase. Auton Neurosci Basic Clin. 29 febbraio 2008;138(1–2):64–75.

63. Zhou J, Scherlag BJ, Edwards J, Jackman WM, Lazzara R, Po SS. Gradients of atrial refractoriness and inducibility of atrial fibrillation due to stimulation of ganglionated plexi. J Cardiovasc Electrophysiol. gennaio 2007;18(1):83–90.

64. Fedele L, Brand T. The Intrinsic Cardiac Nervous System and Its Role in Cardiac Pacemaking and Conduction. J Cardiovasc Dev Dis. 24 novembre 2020;7(4):E54.

65. Cook L, Perry M, Hill A, Thorpe J. Methods to model epicardial adipose tissue-mediated atrial fibrillation. Npj Cardiovasc Health. 26 giugno 2025;2(1):29.

66. Ernault AC, Verkerk AO, Bayer JD, Aras K, Montañés-Agudo P, Mohan RA, et al. Secretome of atrial epicardial adipose tissue facilitates reentrant arrhythmias by myocardial remodeling. Heart Rhythm. settembre 2022;19(9):1461–70.